

Free-breathing motion-informed locally low-rank quantitative 3D myocardial perfusion imaging

Tobias Hoh¹ | Valery Vishnevskiy¹ | Malgorzata Polacin^{1,2} | Robert Manka^{1,2,3} | Maximilian Fuetterer¹ | Sebastian Kozerke¹

¹Institute for Biomedical Engineering, University and ETH Zurich, Zurich, Switzerland

²Institute of Diagnostic and Interventional Radiology, University Hospital Zurich, University of Zurich, Zurich, Switzerland

³Department of Cardiology, University Heart Center, University Hospital Zurich, University of Zurich, Zurich, Switzerland

Correspondence

Sebastian Kozerke, Institute for Biomedical Engineering, University and ETH Zurich, Gloriastrasse 35, Zurich 8092, Switzerland.

Email: kozerke@biomed.ee.ethz.ch

Funding information

Innosuisse - Schweizerische Agentur für Innovationsförderung, Grant/Award Number: 31010.1

Purpose: To propose respiratory motion-informed locally low-rank reconstruction (MI-LLR) for robust free-breathing single-bolus quantitative 3D myocardial perfusion CMR imaging. Simulation and in-vivo results are compared to locally low-rank (LLR) and compressed sensing reconstructions (CS) for reference.

Methods: Data were acquired using a 3D Cartesian pseudo-spiral in-out k-t undersampling scheme ($R = 10$) and reconstructed using MI-LLR, which encompasses two stages. In the first stage, approximate displacement fields are derived from an initial LLR reconstruction to feed a motion-compensated reference system to a second reconstruction stage, which reduces the rank of the inverse problem. For comparison, data were also reconstructed with LLR and frame-by-frame CS using wavelets as sparsifying transform (ℓ_1 -wavelet). Reconstruction accuracy relative to ground truth was assessed using synthetic data for realistic ranges of breathing motion, heart rates, and SNRs. In-vivo experiments were conducted in healthy subjects at rest and during adenosine stress. Myocardial blood flow (MBF) maps were derived using a Fermi model.

Results: Improved uniformity of MBF maps with reduced local variations was achieved with MI-LLR. For rest and stress, intra-volunteer variation of absolute and relative MBF was lower in MI-LLR (± 0.17 mL/g/min [26%] and ± 1.07 mL/g/min [33%]) versus LLR (± 0.19 mL/g/min [28%] and ± 1.22 mL/g/min [36%]) and versus ℓ_1 -wavelet (± 1.17 mL/g/min [113%] and ± 6.87 mL/g/min [115%]). At rest, intra-subject MBF variation was reduced significantly with MI-LLR.

Conclusion: The combination of pseudo-spiral Cartesian undersampling and dual-stage MI-LLR reconstruction improves free-breathing quantitative 3D myocardial perfusion CMR imaging under rest and stress condition.

KEYWORDS

3D perfusion imaging, compressed sensing, dual sequence, single bolus, first-pass myocardial perfusion imaging, free-breathing, low-rank reconstruction, myocardial perfusion quantification

1 | INTRODUCTION

The clinical utility and value of dynamic contrast-enhanced myocardial first-pass perfusion imaging has been demonstrated in a number of landmark trials.¹⁻³ While in today's clinical use, image data are mostly assessed visually or semi-quantitatively to identify ischemia, quantitative approaches⁴ have gained momentum with recent technical advances in data acquisition, reconstruction, and processing.⁵⁻⁸

In contrast to conventional dynamic multi-slice 2D imaging sequences, 3D approaches with whole-heart coverage allow data acquisition in a single time window per cardiac cycle.⁹ The potential clinical value of robust 3D myocardial perfusion imaging relates, in particular, to the ability to quantify the relative ischemic myocardial volume.^{10,11} In view of the increasing utilization of ischemic burden as a marker for decision making for revascularization in stable coronary artery disease,¹² added value has been indicated. Moreover, the importance of quantification of myocardial blood flow (MBF) and related parameters has been emphasized in the context of triple vessel coronary artery disease,^{13,14} microvascular disease,^{15,16} and other conditions.¹⁷

Dynamic 3D perfusion methods require substantial scan acceleration in order to accommodate data sampling into a sufficiently short acquisition window per cardiac cycle. To this end, k-t undersampling in conjunction with k-t BLAST, k-t SENSE,¹⁸⁻²⁰ and k-t PCA^{21,22} has initially been deployed and demonstrated in the clinical setting for various applications and compared against reference standards in single^{10,11,23-25} and multi-center trials.^{26,27} Dedicated advances to improve the reconstruction accuracy from undersampled multi-slice 2D or 3D Cartesian,²⁸⁻³⁰ radial³¹⁻³⁶ and spiral³⁷⁻⁴⁰ k-space trajectories have been proposed. Work on 3D Cartesian,²² radial stack-of-stars,^{41,42} and spirals⁴³ has demonstrated improvements with impact on quantitative perfusion parameters. The ramification of spatiotemporal fidelity on quantitative perfusion indices has been investigated and quantified.⁴⁴

A challenge with k-t reconstruction, however, relates to the requirement to ensure sufficient spatiotemporal data correlations. Therefore, data acquisition is typically conducted in a breathhold, which has been limiting, in particular, during adenosine-induced stress. In order to increase patient comfort and compliance, initial research has been directed to enable free-breathing 3D data acquisition based on Cartesian³⁰ and stack-of-stars undersampling.³⁵

To address respiratory motion of free-breathing data acquisition, approaches applying global or local registration in the image domain have been described. To address challenges due to the dynamic contrast enhancement,

image signal separation into low-rank and sparse components followed by model-based registration has been proposed.⁴⁵ It is noted, however, that 2D registration-based methods can inherently only correct for in-plane and not continuous through-slice motion.

In addition to image-domain registrations, radial self-gating and respiratory motion binning have been used^{42,46-48} to restrict or sort data to different respiratory states. However, retrospective binning of spokes into breathing and heart phases is only applicable for moderate undersampling or continuous acquisition schemes.^{42,49}

In general, nonrigid motion, corrupting the data, can be corrected for using an approximate solution given an estimated motion field.⁵⁰ If rigid motion is assumed, it can be compensated for by application of linear phase shifts in k-space as demonstrated for perfusion imaging.⁵¹

Motion correction has become an important step to improve the conditioning of iterative image reconstruction methods.^{30,52,53} Block low-rank sparsity tracking (BLOSM) has proved beneficial,⁵³ and has been extended to reconstruct from continuously acquired radial, simultaneous multi-slice, heart-phase resolved data.⁴² Similar methods have also been used in computed tomography perfusion imaging⁵⁴ and in other MR applications such as MR parameter mapping⁵⁵ and MR fingerprinting.⁵⁶

For quantification of perfusion data, a dual-sequence, single-bolus approach is desirable.^{28,41,57} The arterial input function (AIF) is preferably recorded in the ascending aorta in an interleaved fashion.⁵⁸

The present study proposes and validates a 3D motion correction approach for locally low-rank (LLR) image reconstruction of Cartesian pseudo-spiral in-out k-t undersampled single-bolus first-pass perfusion data. The method is referred to as respiratory motion-informed locally low-rank reconstruction (MI-LLR). It is shown that, by incorporating a transformation displacement field for each dynamic frame, MI-LLR is able to correct for non-rigid in- and through-plane organ motion during rest and stress. Numerical simulations and phantom experiments are used to demonstrate the robustness of the MI-LLR approach with respect to cardiac and breathing motion in comparison to LLR⁵⁵ and frame-by-frame compressed sensing (CS) using wavelets as sparsifying transform (ℓ_1 -wavelet)^{59,60} reconstructions. In-vivo feasibility of the proposed method is assessed in subjects during rest and stress condition.*

2 | METHODS

2.1 | Image acquisition

A dynamically interleaved 2D/3D dual-sequence, single-bolus scheme was implemented on a clinical

1.5T MR system based on an electrocardiogram (ECG)-triggered saturation-recovery spoiled gradient echo sequences with T_1 - and B_1 -insensitive saturation preparation pulses⁶² as described previously.²⁸

As shown in Figure 1A, the 3D perfusion scan is triggered to end systole. The 2D AIF images are acquired in the ascending aorta during diastole. A pseudo-spiral Cartesian undersampling pattern was implemented as illustrated in Figure 1B,C. The sampling distribution was defined by a variable density function⁶³ with an elliptical k-space shutter as depicted in Figure 1B. For each dynamic imaging frame, k-space profiles were chosen according to the density distribution while avoiding profile duplication. At the k-space center, a 2×4 k_z - k_y area was fully sampled. The temporal order of profiles was according to a spiral-in—spiral-out scheme, placing the k-space center and the nominal saturation delay at half the acquisition time (Figure 1C). Imaging parameters were: TR/TE = 2.0/1.0 ms, spatial resolution: $2.5 \times 2.5 \times 10$ mm³, FOV: $300 \times 300 \times 100$ mm³, covering the full ventricle from apex to base, flip angle: 15° , acquisition window: 240 ms, saturation delay: 135 ms, undersampling factor $R = 10$.

For the interleaved acquisition of the AIF, a fully sampled center-out Cartesian pattern was used with spatial resolution: 10×10 mm², slice thickness: 15 mm, flip angle: 15° , acquisition window: 56–64 ms, saturation delay: 30 ms. TR and TE were set equal to the corresponding 3D sequence to avoid different T_1 and T_2^* weightings.

All images were acquired on a 1.5T Philips Achieva MR system (Philips Healthcare, Best) using a five-element cardiac receive coil array. Gadobutrol (Gadovist, Bayer Schering Pharma) was used as contrast agent (CA).

2.2 | Image reconstruction and motion compensation

Conventional LLR reconstruction⁵⁵ leverages spatio-temporal correlation of imaging data by penalizing the nuclear norms of patch matrices stacked along time. For zero-filled k-space data $\mathbf{S} \in \mathbb{C}^{N_s N_c \times T}$ with T dynamics, N_c coils, containing N_s k-space samples each, LLR reconstructed image data $\mathbf{I}_{\text{LLR}} \in \mathbb{C}^{N_v \times T}$ of N_v voxels is achieved by solving the following convex optimization problem⁵⁵:

$$\mathbf{I}_{\text{LLR}} = \underset{\mathbf{I}}{\operatorname{argmin}} \|\mathbf{\Omega} \mathcal{F} \mathbf{C} \mathbf{I} - \mathbf{S}\|_2^2 + \lambda_{\text{LLR}} \sum_{b \in \mathbf{U}} \|\mathbf{P}_b \mathbf{I}\|_* \quad (1)$$

with the undersampling operator $\mathbf{\Omega} \in \{0, 1\}^{N_s N_c \times N_s N_c}$, Fourier transform $\mathcal{F} \in \mathbb{C}^{N_s N_c \times N_v N_c}$, coil sensitivities $\mathbf{C} \in \mathbb{C}^{N_c N_v \times N_v}$ and regularization weight λ_{LLR} . The patch extraction operator $\mathbf{P}_b \in \{0, 1\}^{n_x n_y n_z \times N_v}$ refers to the b -th patch,

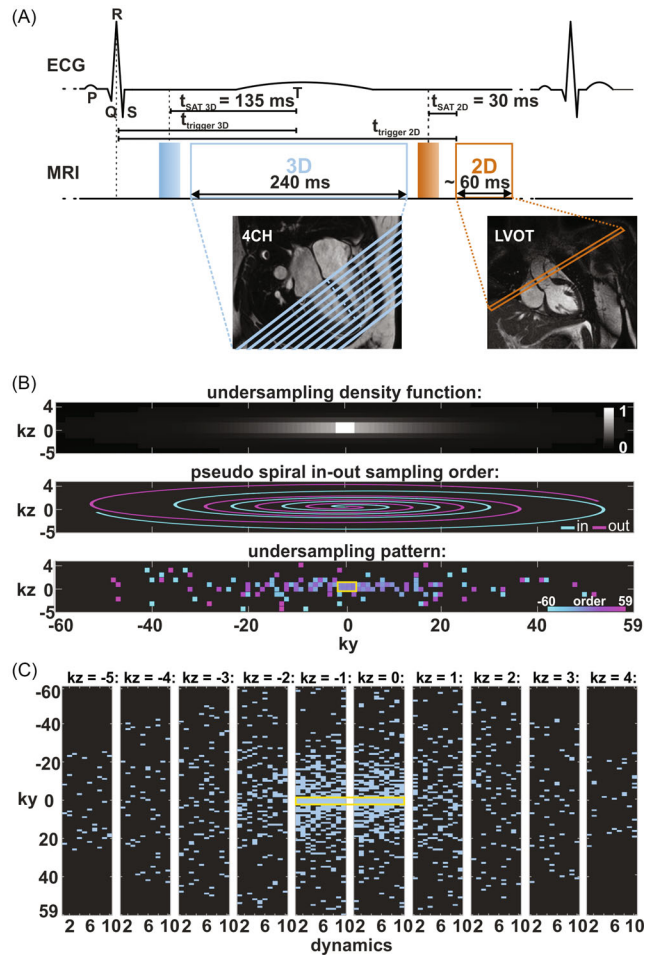


FIGURE 1 Data acquisition. A, Dual-sequence diagram with corresponding ECG trace and typical planning of the 3D and 2D stacks. The 3D perfusion scan is triggered to end systole, the 2D arterial input function (AIF) images to diastole. The 3D volume is sampled by the proposed undersampled pseudo-spiral in-out Cartesian trajectory, while linear center-out Cartesian sampling is used for the 2D AIF slice. B, The 3D data acquisition scheme. Data are sampled using a volumetric pseudo-spiral Cartesian sampling pattern. Undersampling density function (top), idealised spiral-in-out trajectory (middle), exemplary 10-fold undersampling pattern (bottom). C, Resulting k_y - k_z sampling pattern after 10 dynamics. The yellow rectangle highlights the densely sampled k-space center

where \mathbf{U} is a set of patch indices, with patch size of $n_x \times n_y \times n_z$ voxels. In each iteration, patches are selected randomly to avoid blocking artefacts. The optimization problem (Equation 1) is posed in the synthesis form⁶⁴ and, therefore, solved with Nesterov-accelerated proximal gradient descent.⁶⁵

For the first stage of MI-LLR reconstruction, approximate displacement fields are derived to feed a motion-compensated reference system to a second reconstruction stage, allowing to reduce the rank of the inverse problem. Therefore, the initial reconstruction

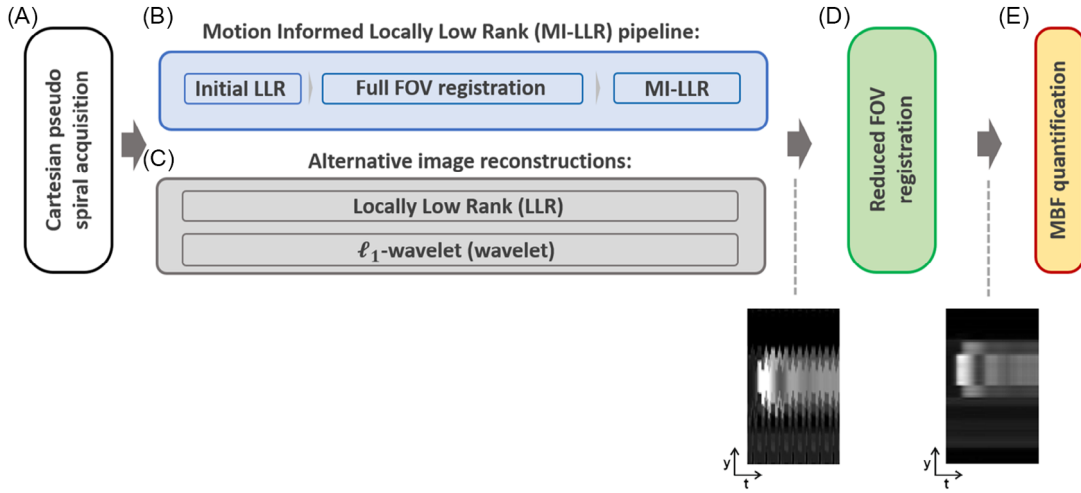


FIGURE 2 The 3D data acquisition and reconstruction steps. A, Data acquisition using the Cartesian 10-fold accelerated spiral-in—spiral-out acquisition pattern. B, The motion-informed locally low-rank reconstruction (MI-LLR) pipeline: Patch-based initial LLR reconstruction followed by full FOV registration. Resulting deformation field allows to regularize over motion states for MI-LLR. C, Alternative image reconstructions using LLR and a frame by frame ℓ_1 -wavelet (wavelet) reconstruction. After step B and D, 3D image series still contain motion as indicated by the intensity-time profiles and require registration in the reduced FOV around the heart (D) in order to perform myocardial blood flow (MBF) quantification (E). Please note: The MI-LLR reconstruction pipeline is also further detailed in Supporting Information Figure S1

$\mathbf{I}_{\text{LLR}} = [\mathbf{i}_1, \dots, \mathbf{i}_T]$ is then registered across T dynamics using the pTV registration toolbox.⁶⁶ Group-wise image registration is achieved by minimizing the nuclear image dissimilarity metric of warped images $\mathbf{i}_t \circ \mathbf{d}_t$ stacked over time $\|\mathbf{i}_1 \circ \mathbf{d}_1, \dots, \mathbf{i}_T \circ \mathbf{d}_T\|_*$,⁶⁷ where displacement fields $\mathbf{d}_t = \mathbf{d}_t(\mathbf{d}'_t)$ are parametrized by first-order B-spline coefficients \mathbf{d}'_t with a cell width of five voxels in each spatial dimension:

$$[\mathbf{d}'_1, \dots, \mathbf{d}'_T] = \underset{[\mathbf{d}'_1, \dots, \mathbf{d}'_T]}{\operatorname{argmin}} \|\mathbf{i}_1 \circ \mathbf{d}_1, \dots, \mathbf{i}_T \circ \mathbf{d}_T\|_* + \lambda_{\text{VTV}} \sum_{pt} \sqrt{\sum_{jk} (\nabla_k \mathbf{d}'_j)_{pt}^2}. \quad (2)$$

The regularization weight λ_{VTV} penalizes the vectorial total variation (VTV),⁶⁸ which imposes group sparsity over displacement component j in direction k for each spatio-temporal voxel location (p, t) .

Displacements fields \mathbf{d}_j , estimated by image registration, map acquired images into a common reference frame. To pose the second stage of the MI-LLR reconstruction problem in the synthesis form,⁶⁴ the displacement fields are inverted using linear interpolation: $\mathbf{q}_t \approx \mathbf{d}_t^{-1}$. Hence, corresponding linear operators $\mathbf{Q}_t \mathbf{i}_t = \mathbf{Q}_t(\mathbf{q}_t) \mathbf{i}_t = \mathbf{i}_t \circ \mathbf{q}_t$ were used to map a fixed reference frame to the target configuration t :

$$\mathbf{I}_{\text{MI-LLR}} = \underset{\mathbf{I}}{\operatorname{argmin}} \left\| \Omega \mathcal{F} \mathbf{C} [\mathbf{Q}_1 \mathbf{i}_1, \dots, \mathbf{Q}_T \mathbf{i}_T] - \mathbf{S} \right\|_2^2 + \lambda_{\text{MI-LLR}} \sum_{b \in \mathbf{U}} \|\mathbf{P}_b \mathbf{I}\|_*. \quad (3)$$

Here, $\lambda_{\text{MI-LLR}}$ weights LLR regularization in the motion-compensated configuration, while $\mathbf{Q}_t \mathbf{i}_t$ for $t = 1, \dots, T$ represents the original image sequence defined by the k-spaces \mathbf{S} . Since image warping operators \mathbf{Q}_t are applied in the data term, this optimization problem is convex and formulated in the synthesis form allowing to use the Nesterov-accelerated proximal gradient descent.⁶⁵ The algorithm was implemented in Matlab (Mathworks) on GPUs.

Sensitivity maps for coil calibration were estimated from reference scans using the ESPiRiT method.⁶⁹ Imaging data from the scanner were extracted and pre-processed using MRecon (Gyro Tools LLC).

The entire framework is schematically outlined in Figure 2A–E. At first, data are acquired using the Cartesian pseudo spiral acquisition and put into the MI-LLR reconstruction, which encompasses two stages. In the first stage (Figure 2B), images are reconstructed using LLR (Equation 1) with a patch size of $n_x = n_y = n_z = 12$ and underregularization to capture spatiotemporal image variations ($\lambda_{\text{LLR}} = 0.05$). While the images show residual undersampling artefacts, motion patterns are not suppressed and visible. These images are registered using Equation (2) with regularization weight $\lambda_{\text{VTV}} = 0.001$ on the displacements to suppress the impact of residual aliasing artefacts in the initial LLR reconstruction. Thereafter, estimated displacement fields are used to perform the second stage of the MI-LLR reconstruction according to Equation (3), thereby allowing to reduce the regularization weight. The MI-LLR pipeline is illustrated for a

representative case in Supporting Information Figure S1, which is available online.

For alternative reconstructions (Figure 2C), LLR and ℓ_1 -wavelet (wavelet), referring to CS reconstruction using wavelets as sparsifying transform and sensitivity encoding (i.e., SPARSE-SENSE),^{59,60,63,70,71} were used. Image data $\mathbf{I}_{\text{wavelet}} \in \mathbb{C}^{N_v \times T}$ of N_v voxels was obtained by solving:

$$\mathbf{I}_{\text{wavelet}} = \underset{\mathbf{I}}{\operatorname{argmin}} \|\mathbf{\Omega} \mathcal{F} \mathbf{C} \mathbf{I} - \mathbf{S}\|_2^2 + \lambda_{\text{wavelet}} \|\mathbf{D} \mathbf{I}\|_1 \quad (4)$$

where \mathbf{D} is the discrete Daubechies wavelet transform. Equation (4) was solved using the Berkeley advanced reconstruction toolbox (BART).⁷²

For in-vivo image reconstructions, the minimum values of the regularization parameters $\lambda_{\text{MI-LLR}}$ and λ_{LLR} , which suppress background signal variation to 0.05% of the maximum image intensity, were chosen using a grid search approach and were $\lambda_{\text{MI-LLR}} \sim 0.30$ and $\lambda_{\text{LLR}} \sim 0.40$. The regularization parameter of the ℓ_1 -wavelet reconstruction λ_{wavelet} was set to 0.01. For synthetic experiments, optimal regularization parameters, yielding the lowest reconstruction error, were found using a grid search and were $\lambda_{\text{MI-LLR}} \sim 0.25$, $\lambda_{\text{LLR}} \sim 0.30$, and $\lambda_{\text{wavelet}} \sim 0.01$.

2.3 | Postprocessing and MBF quantification

Reconstructed 3D data were zero-filled to $1.25 \times 1.25 \times 5 \text{ mm}^3$ and 2D-AIF images were zero-filled to $2.5 \times 2.5 \text{ mm}^2$. All image series were registered to compensate for residual motion prior to signal post-processing. Signal post-processing and perfusion quantification were conducted in Matlab (Mathworks). For local myocardial perfusion mapping, the images were convolved using the following kernel: $\frac{1}{5}[0, 1, 0; 1, 1, 1; 0, 1, 0]$ to reduce noise at the cost of resolution.

The myocardium was segmented across the 10 slices and divided into six circumferential sectors per slice. Local and sector-wise myocardial signal time curves were derived along with the AIF.

Given the signal model of the saturation recovery Cartesian sequence, $T_1(t)$ translates to signal $I(t)$ as^{73,74}:

$$I(t) = I_0 \cdot \left[\left(1 - \exp\left(-\frac{T_{\text{sat}}}{T_1(t)}\right) \right) \cdot a(t)^{n-1} + \left(1 - \exp\left(-\frac{\text{TR}}{T_1(t)}\right) \right) \cdot \frac{1 - a(t)^{n-1}}{1 - a(t)} \right]$$

with

$$a(t) = \exp\left(-\frac{\text{TR}}{T_1(t)}\right) \cos \alpha \quad (5)$$

with the baseline signal for fully relaxed magnetization I_0 , saturation delay T_{sat} , repetition time TR, flip angle α , the number of profiles sampled until k-space center n . Accordingly, $T_1(t)$ was calculated for every dynamic t for the myocardium as well as in the ascending aorta. Concentration-time curves $c(t)$ were derived using:

$$c(t) = \frac{T_{1,0} - T_1(t)}{T_1(t) \cdot T_{1,0} \cdot r} \quad (6)$$

where $T_{1,0}$ refers to the native T_1 relaxation time and r to the specific CA relaxivity (gadobutrol: $r = 5.2 \text{ L/mmol} \cdot \text{s}$). Accordingly, MBF was quantified using $c_{\text{MYO}}(t)$ and $c_{\text{AIF}}(t)$ based on a Fermi model⁷⁴:

$$c_{\text{MYO}}(t) = \text{IRF}_{\text{Fermi}}(t) * c_{\text{AIF}}(t),$$

with

$$\text{IRF}_{\text{Fermi}}(t) = \text{MBF} \cdot \frac{1 - \nu}{1 - \nu \cdot \exp(-\mu t)} \cdot \Theta(t - t_{\text{shift}}) \quad (7)$$

with fitting parameters ν , μ that entail no physiological meaning and the Heaviside step function Θ , with the time difference between AIF and myocardial signal given by t_{shift} . The parameters of interest were fitted in the least square sense. To determine the global myocardial and blood $T_{1,0}$ a MOLLI scan⁷⁵ was used. Further details of the implementation of the deconvolution and estimation process are outlined in.²⁸

2.4 | Simulation studies

Numerical simulations were performed to validate the MI-LLR framework. A fully sampled free-breathing 3D perfusion numerical phantom was created using the signal model given in Equation (5) based on the MRXCAT simulation framework.⁷⁶ Spatial resolution of the ground truth (GT) phantom was $1.25 \times 1.25 \text{ mm}^2$, slice thickness: 5 mm, 20 slices. To introduce partial volume effects, the GT object was subsequently downsampled to yield the final phantom parameters: $2.5 \times 2.5 \times 10 \text{ mm}^3$, 10 slices, TR/TE: 2.0/1.0 ms, flip angle: 15°, CA dose: 0.075 mmol/kg body weight (b.w.), five receive coils, MBF: 3.5 mL/g/min, 70 simulated heart beats, $R = 10$. The numerical phantom was further modified to include cardiac and respiratory motion during readout to investigate the effects of motion on reconstruction and MBF estimation. Heart rates between 60 and 120 bpm and respiratory motion based on in-vivo navigator data with maximum amplitudes of 25 and 40 mm as provided in the supporting material (Supporting Information Figure S2) were simulated.

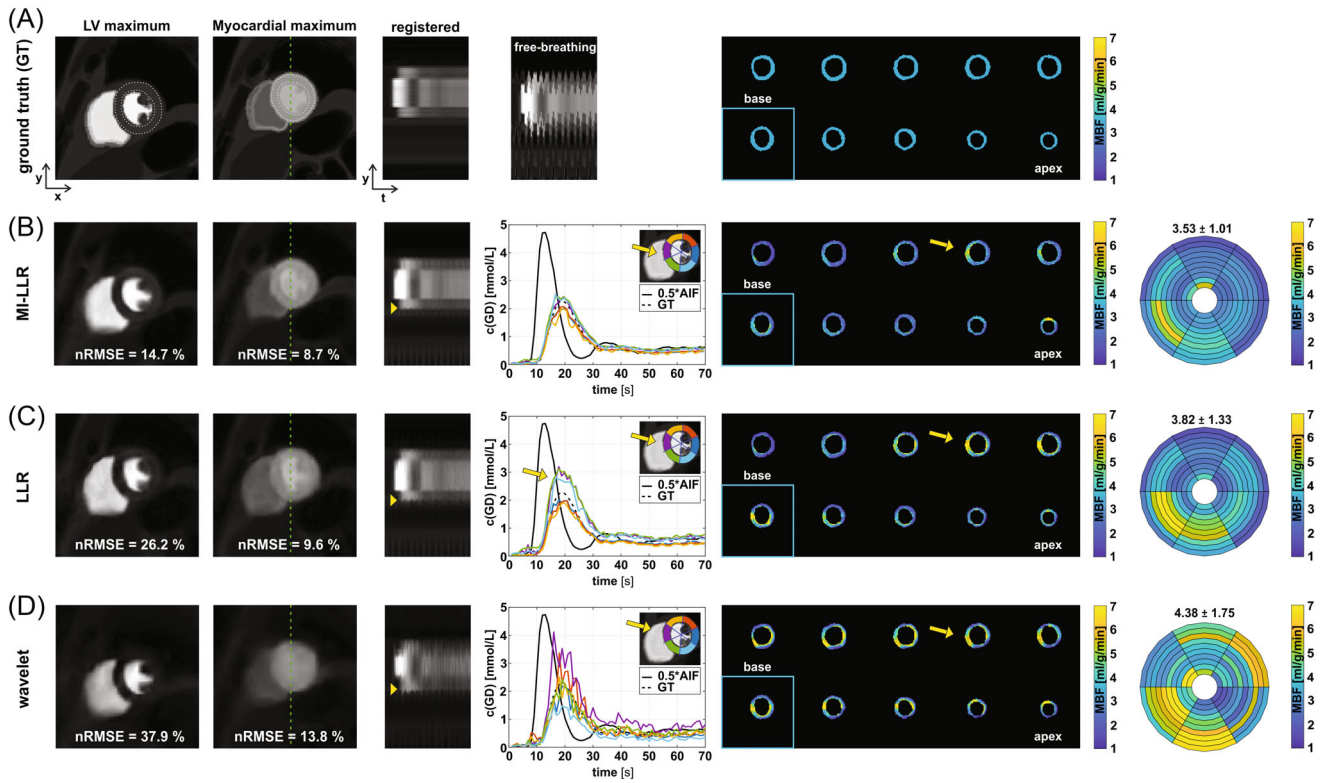


FIGURE 3 Simulation results for synthetic stress data at a heart rate of 60 bpm and 25 mm respiratory amplitude. GT (A) and the proposed motion-informed locally low-rank reconstruction (MI-LLR) (B), LLR (C), and ℓ_1 -wavelet (wavelet) (D). The panels show (horizontal order), for a midventricular slice, reconstruction results and errors (nRMSEs) at peak LV and peak myocardial signal in the myocardial region as indicated by white dashed masks, intensity-time profiles upon motion correction with displacement fields obtained from registration of GT image series (for reference, GT profiles are shown for the registered and the free-breathing case), concentration-time curves, for all slices, myocardial blood flow (MBF) maps, and regional means with MBF \pm SD, respectively

In order to analyze the simulation results, the normalized RMS error (nRMSE) of reconstructed magnitude images with respect to GT images in the masked myocardial region of interest (respective masks are indicated in Figure 3A) were calculated according to:

$$\text{nRMSE} = \sqrt{\frac{\sum_{\tilde{p} \in \text{mask}} |\mathbf{I}(\tilde{p}) - \mathbf{I}_{\text{GT}}(\tilde{p})|^2}{N_{\text{mask}} * \max(\mathbf{I}_{\text{GT}}(\tilde{p})^2)}} \quad (8)$$

where N_{mask} corresponds to the number of pixels \tilde{p} in the myocardial mask.

MBF data derived from reconstructed images were compared to MBF values from GT. Reconstructed image data were registered using the displacement fields obtained from registration of the GT image series to avoid confounding effects of the final registration step on MBF accuracy. Quantification errors were evaluated as mean absolute error (MAE) \pm 1 SD of the absolute error over all myocardial pixels from 10 slices of the 3D volume,

calculated according to:

$$\text{MAE} = \frac{\sum_{\tilde{p} \in \text{mask}} |\text{MBF}(\tilde{p}) - \text{MBF}_{\text{GT}}(\tilde{p})|}{N_{\text{mask}}} \quad (9)$$

where N_{mask} corresponds to the number of myocardial pixels \tilde{p} in the masked 3D volume. To investigate the effects of SNR on MBF quantification accuracy, different noise levels were added to simulated data at resting heart-rate, i.e., 60 bpm, and 25 mm respiratory motion amplitude.

Statistical differences were assessed using the two tailed Student's t -test; $p < 0.05$ was considered significant.

2.5 | Phantom studies

To verify the signal to concentration conversion after image acquisition and reconstruction, tubes were filled with purified water and doped with different concentrations of gadobutrol (from 0 to 2.25 mmol/L). The detailed

setup of the phantom validation is summarized in Figure 5. The tubes were inserted into a cylindrical Agar phantom. Concentrations were sequentially varied to mimic the CA dynamics in the left ventricle and in myocardium by manually replacing tubes in between subsequent measurements. Concurrently, the phantom was displaced laterally to four positions with a maximum displacement of 30 mm to mimic in-vivo breathing motion dynamics.

2.6 | In-vivo experiments

Twelve healthy volunteers (7 male) with an average age 25.2 ± 2.4 y underwent first-pass rest perfusion examinations; 7 underwent a rest and stress protocol. All volunteers were scanned upon written informed consent according to local ethics regulations. Two contrast-enhanced dual-sequence imaging experiments were run using CA boluses at doses of 0.075 mmol/kg b.w. to compare imaging at rest and stress. CA was injected at 4 mL/s and followed by a 30 mL saline flush at the same rate using a power injector (Medrad). Fifteen minutes were allowed for CA washout in-between the two bolus injections; stress imaging was always performed first. Adenosine (Kanton-sapotheke, University Hospital Zurich) was injected for at least 3 min at doses of 140 μ g/kg b.w./min under continuous monitoring of heart rate and blood pressure in accordance with standard clinical practice. Image acquisition covered 80 heartbeats during free breathing of the subject.

MI-LLR images, intensity-time profiles, concentration-time curves and resulting MBF maps were compared to LLR and ℓ_1 -wavelet reconstructions for reference.

3 | RESULTS

3.1 | Simulation studies

Comparing MI-LLR to LLR and ℓ_1 -wavelet reconstructions, image error was found to be reduced as shown by images at left-ventricular (LV) and myocardial (Myo) peak signal (Figure 3) with reconstruction nRMSEs for MI-LLR of 14.7% (LV) and 8.7% (Myo) versus LLR (26.2% and 9.6%) and ℓ_1 -wavelet (37.9% and 13.8%). Intensity-time profiles indicate improved motion compensation with MI-LLR relative to LLR as indicated by yellow markers (Figure 3B,C). Concentration-time curves of the six sectors reflect improved motion compensation of the myocardium. In particular, septal sectors show reduced signal variance with MI-LLR when compared to LLR

and ℓ_1 -wavelet. For MI-LLR, local and sector-wise MBF maps reveal more uniform values of 3.53 ± 1.01 mL/g/min with MI-LLR when compared to 3.82 ± 1.33 mL/g/min with LLR and 4.38 ± 1.75 mL/g/min with ℓ_1 -wavelet. MBF maps generally show MBF overestimation which is, however, reduced with MI-LLR when compared to LLR and ℓ_1 -wavelet.

In Figure 4 reconstruction nRMSE and mean absolute error (MAE) of MBF as a function of heart rate, respiratory amplitude, and SNR are reduced with MI-LLR when compared to LLR and ℓ_1 -wavelet. Heart rate dependencies for 25 and 44 mm peak respiratory amplitude show reduced reconstruction nRMSEs and MBF MAEs of MI-LLR when compared to LLR (Figure 4A,B,D,E). With a peak respiratory amplitude of 25 mm, median reconstruction nRMSEs for MI-LLR varied from 7.9% to 8.5%, while LLR shows higher median reconstruction nRMSEs (8.8%–9.5%), as does ℓ_1 -wavelet (13.5%–13.4%). Reduced MBF MAEs resulted with MI-LLR (1.25–1.44) as compared to LLR (1.55–1.61) and ℓ_1 -wavelet (2.39–2.86) up to a heart rate of 120 bpm. As summarized in Table 1, regional MBF showed significantly reduced variation with MI-LLR ($\pm 30\%$) as compared to LLR ($\pm 38\%$) and ℓ_1 -wavelet ($\pm 45\%$). With a peak respiratory amplitude of 40 mm, MI-LLR yielded reduced median nRMSEs of 8.7%–8.9% when compared to 8.8%–9.3% for LLR and 13.1%–13.2% for ℓ_1 -wavelet; reduced MBF MAEs are seen with MI-LLR (1.25–1.44) when compared to LLR (1.89–2.03) and ℓ_1 -wavelet (3.05–3.14). Regional MBF showed significantly reduced variation for MI-LLR ($\pm 38\%$) when compared to LLR ($\pm 44\%$) and ℓ_1 -wavelet ($\pm 44\%$). The SNR dependence demonstrates improved performance of MI-LLR when compared to LLR; median reconstruction nRMSEs decreased from 10.1% to 8.1% for MI-LLR when compared to 10.8%–9.0% for LLR, and 14.5%–13.4% for ℓ_1 -wavelet when increasing SNR from 12 to 37 (Figure 4C); likewise reduced MBF MAE is seen with MI-LLR (1.38–1.07) when compared to LLR (3.11–2.44) and ℓ_1 -wavelet (3.73–3.17) with reduced regional MBF variation for MI-LLR ($\pm 34\%$) as compared to LLR ($\pm 53\%$) and ℓ_1 -wavelet ($\pm 52\%$).

The average motion accuracy after the final registration step was 1.96 and 2.18 mm for 25 and 40 mm breathing amplitude, respectively. After registration, differences in motion accuracy between MI-LLR and LLR were insignificant.

3.2 | Phantom studies

Reconstruction results for the proposed method are shown in Figure 5. Exact signal to concentration conversion is

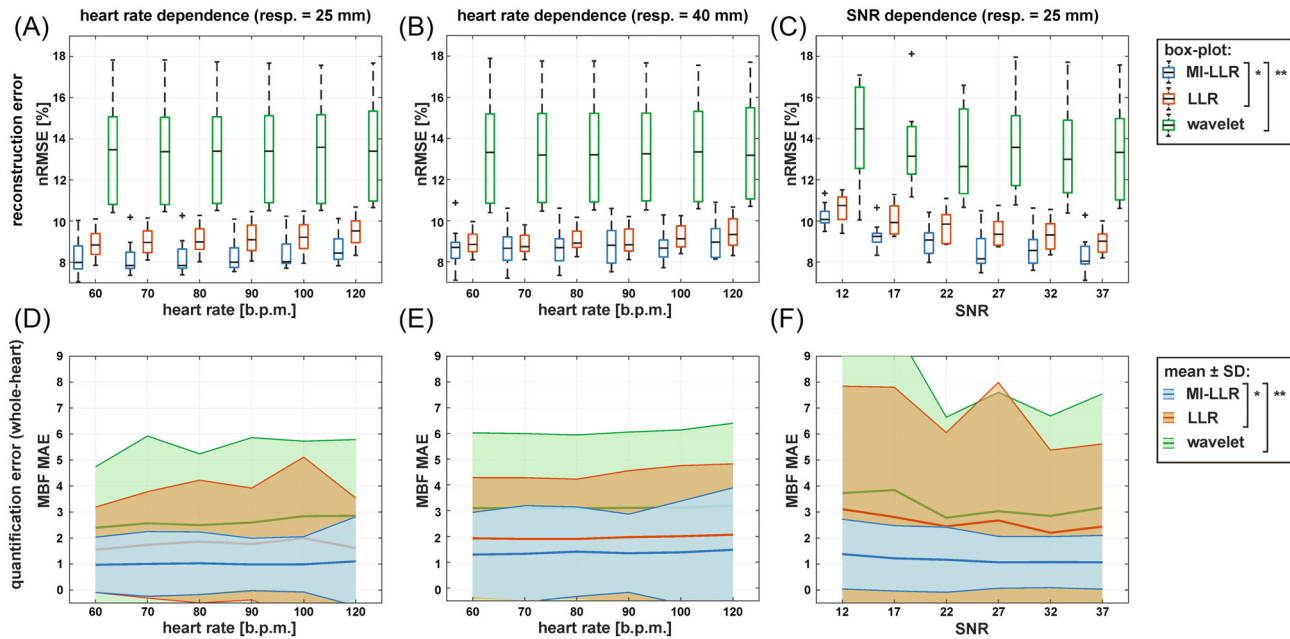


FIGURE 4 Simulation results comparing reconstruction nRMSE (A–C) and myocardial blood flow (MBF) MAE (D, E) for motion-informed locally low-rank (MI-LLR) versus LLR and ℓ_1 -wavelet (wavelet) for heart rates from 60 to 120 bpm for respiration amplitudes of 25 mm (A, D) and 40 mm (B, E), and as a function of SNR (C, F). The boxplots summarize reconstruction nRMSE over 10 slices at myocardial peak signal. Shaded areas in (D–F) indicate 1 SD (SD) of MBF over all pixels from all 10 slices. To enhance representation, shaded areas are not shown for MAE < 0.5. Significant differences ($p < 0.05$) are marked by asterisks: * Refers to significant reduction when MI-LLR is compared relative to LLR. ** refers to significant reduction when MI-LLR or LLR are compared relative to ℓ_1 -wavelet (wavelet). For amplitudes of 25 mm, 40 mm, and SNR, all * $p < 0.001$, ** $p < 0.001$

examined by comparison of reference to measured concentration with a linear regression model. Figure 5D shows the CA concentrations derived from T_1 values measured with the proposed 3D acquisition and reconstruction. Data are in agreement up to gadolinium concentrations of 2.4 mmol/L as indicated by the slope of linear regression of 1.08 (offset = 0.07).

3.3 | In-vivo studies

In Figures 6 and 7, example reconstruction results for rest and stress acquisitions of a healthy male volunteer (average heart rate 70 bpm [rest] and 81 bpm [stress], navigator displacement 20 mm [rest] and 24 mm [stress]) are reported at peak LV and myocardial contrast maximum, and intensity profiles (videos are included as Supporting Information Videos S1 and S2). At rest, MI-LLR images appear less blurred than LLR at myocardial intensity maximum. Intensity profiles indicate sharper borders between myocardium and blood pool for MI-LLR when compared to LLR. At stress, MI-LLR images appear less blurred than LLR; ℓ_1 -wavelet images show pronounced artefacts. Intensity profiles indicate sharper borders between myocardium and blood pool for MI-LLR as compared to LLR images, with more residual motion seen in the LLR profile, while

ℓ_1 -wavelet intensity profiles are dominated by pronounced signal intensity artefacts.

In Figures 8 and 9, corresponding quantifications are summarized at rest and stress, respectively. At rest, concentration-time curves show residual artefacts for both MI-LLR and LLR. Concentration time curves exhibit reduced fluctuations over time for MI-LLR (signal maximum at 0.47 mmol/L with 0.30 ± 0.06 mmol/L) when compared to LLR (signal maximum at 0.58 mmol/L with 0.32 ± 0.08 mmol/L). Concentration time curves from ℓ_1 -wavelet reconstructions are corrupted by artefacts. Rest maps show uniform MBF values but signal spilling in the basal slices. Apical locations show reduced local MBFs as compared to basal locations. MBF variation are reduced using MI-LLR (± 0.11 mL/g/min) vs. LLR (± 0.13 mL/g/min) versus ℓ_1 -wavelet (± 0.27 mL/g/min).

At stress (Figure 9), concentration-time curves show residual artefacts induced by motion for both MI-LLR and LLR. Signal maxima are lower for MI-LLR (at 0.69 mmol/L with 0.65 ± 0.05 mmol/L) as compared to LLR (at 0.80 mmol/L with 0.69 ± 0.08 mmol/L). MBF maps show uniform MBF values but signal spilling in the basal slices. Apical locations show reduced local MBFs as compared to basal locations. Bulls eye plots indicate that regional means are compromised less with MI-LLR; MBF variation is seen to be significantly reduced ($p < 0.05$) using

TABLE 1 Myocardial blood flow (MBF) quantification metrics for simulation and in-vivo data

MBF quantification metrics		Motion-informed locally low-rank (MI-LLR)	Locally low rank (LLR)	ℓ_1 -wavelet (wavelet)
Simulation	mean MBF \pm SD [ml/g/min] (SD [%]) (ground truth = 3.5 ml/g/min)	3.44 \pm 1.03 (30%)*, **	3.77 \pm 1.43 (38%)*, **	4.04 \pm 1.82 (45%)
	Resp. amplitude: 25 mm, HR: 60–120 bpm			
	Resp. amplitude: 40 mm, HR: 60–120 bpm	3.74 \pm 1.42 (38%)*, **	3.67 \pm 1.62 (44%)*, **	4.59 \pm 2.02 (44%)
In-vivo	Resp. amplitude: 25 mm, SNR: 12–37	3.43 \pm 1.17 (34%)*, **	3.96 \pm 2.10 (53%)*, **	4.44 \pm 2.31 (52%)
	Stress: \pm mean intra-volunteer SD [ml/g/min] (SD [%])	\pm 1.07 (33%)*, **	\pm 1.22 (36%)*, **	\pm 6.87 (115%)
	Mean resp. amplitude \pm SD: 24.9 \pm 7.4 mm Mean HR \pm SD: 87 \pm 9 bpm			
Rest: \pm mean intra-volunteer SD [ml/g/min] (SD [%])	\pm 0.17 (26%)*, **	\pm 0.19 (28%)*, **	\pm 1.17 (113%)	
Mean resp. amplitude \pm STD: 16.3 \pm 9.3 mm Mean HR \pm SD: 67 \pm 7 bpm				

Note: Significant differences ($p < 0.05$) of absolute and relative MBF SD (SD [%]) are marked by asterisks:

* Refers to significant differences when MBF SDs of motion-informed locally low-rank (MI-LLR) are compared relative to LLR.

** Refers to significant differences when MBF SDs of MI-LLR or LLR are compared relative to ℓ_1 -wavelet (wavelet). In-vivo SDs were normalized by the means (SD [%]).

MI-LLR (± 0.70 mL/g/min) vs. LLR (± 0.79 mL/g/min) versus ℓ_1 -wavelet (± 3.36 ml/g/min).

Spatial variation of CA concentration across the myocardium at peak myocardial enhancement for all volunteers is compared in Supporting Information Table S1. MBF quantification results for all subjects are summarized in Table 1 and Supporting Information Figure S3. One subject showed a high response to adenosine stress resulting in heart rates exceeding 130 bpm. Failing ECG gating resulted in triggering of only every second heart-beat. The stress scan was thus excluded from analysis. For MI-LLR reconstruction, at an average resting heart rate of 67 ± 7 bpm, the average inter-volunteer MBF was 0.65 ± 0.22 mL/g/min, while, under stress and an average stress heart rate of 87 ± 9 bpm, the average MBF was 3.23 ± 0.61 mL/g/min compared to 0.68 ± 0.23 mL/g/min (rest) and 3.39 ± 0.34 mL/g/min (stress) for LLR versus 1.03 ± 0.75 mL/g/min (rest) and 5.94 ± 3.98 mL/g/min (stress) for ℓ_1 -wavelet. Intra-volunteer variation of absolute and relative MBF was lower in MI-LLR (± 0.17 mL/g/min [26%] and ± 1.07 mL/g/min [33%]) versus LLR (± 0.19 mL/g/min [28%] and ± 1.22 mL/g/min [36%]) and versus ℓ_1 -wavelet (± 1.17 mL/g/min [113%] and ± 6.87 mL/g/min [115%]), for rest and stress, combined. At rest, the reduction in regional MBF variation between MI-LLR and LLR was significant ($p = 0.0073$); at stress it was insignificant. SDs of MBF values derived from MI-LLR and LLR were significantly reduced when compared to ℓ_1 -wavelet at rest and stress.

4 | DISCUSSION

In this study, a 3D motion-informed locally low-rank image reconstruction framework, combined with Cartesian pseudo-spiral k-t undersampling, was developed and the suitability for robust free-breathing whole-heart quantitative perfusion imaging has been demonstrated under rest and stress conditions in volunteers.

The proposed MI-LLR approach yields qualitative and quantitative improvement compared to LLR reconstruction for free-breathing imaging. In-vivo MBF values derived from both 3D MI-LLR and LLR agree with the range of values reported for quantitative 2D perfusion CMR methods.¹⁷ Reduced variation of regional MBF values was found for MI-LLR when compared to LLR and ℓ_1 -wavelet in simulation and for in-vivo data at rest. Average rest and stress values and their variations compare well to data from other 3D studies.^{28,42,44} Differences between MI-LLR and LLR depend on individual subjects' breathing pattern and heart rates (example cases shown in Supporting Information Figures S5–S8; Supporting Information Videos S3 and S4).

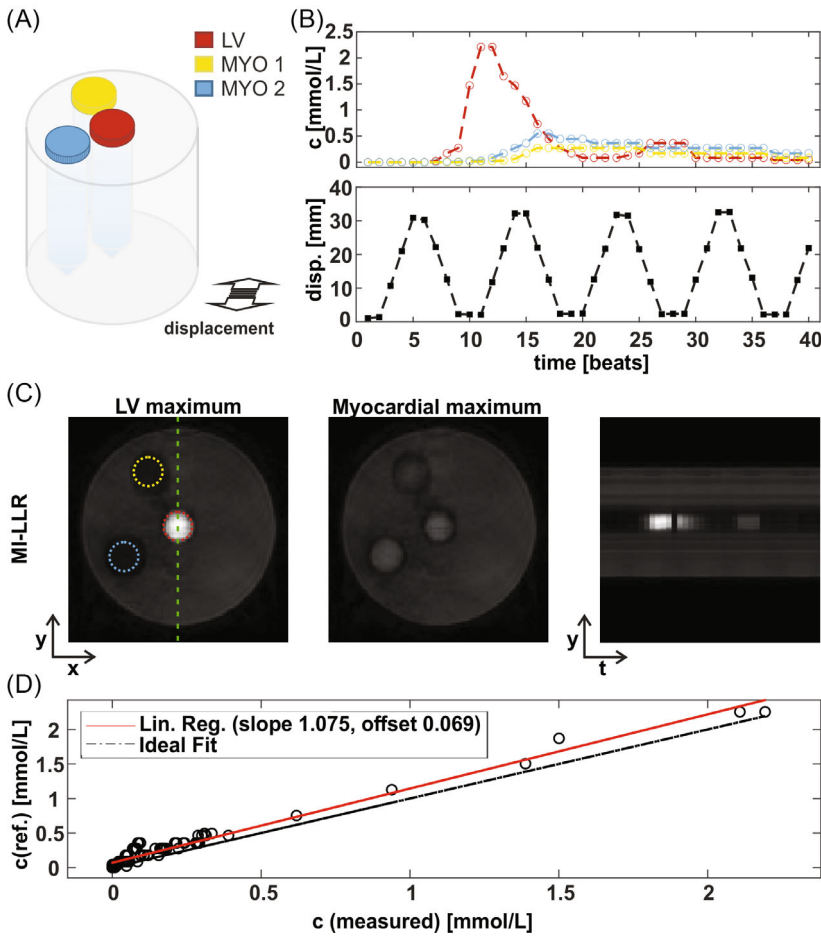


FIGURE 5 Phantom sequence validation. A, Agar phantom holds three sites for falcon tubes filled with saline, doped with various concentrations of gadobutrol. B, The respective concentrations are varied concomitant with a displacement of the phantom, measured with a navigator, in order to reflect the perfusion and breathing dynamics, respectively. C, Resulting motion-informed locally low-rank reconstructions (MI-LLR) at concentrations corresponding to LV and myocardial maximum with respective temporal intensity profile plot. D, Comparison of reference gadolinium concentrations, verified by T_1 mapping, and the measured concentrations obtained with the 3D acquisition scheme

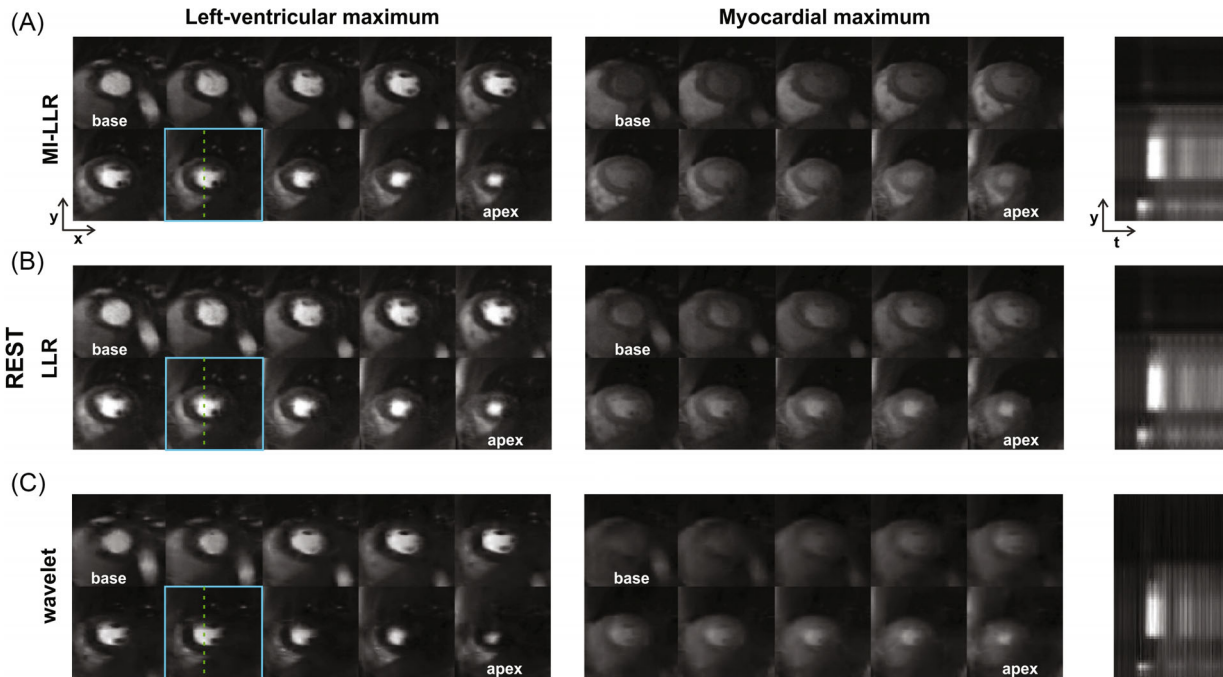


FIGURE 6 In-vivo results for motion-informed locally low-rank (MI-LLR) (A), LLR (B), and ℓ_1 -wavelet (wavelet) (C) during rest condition. Imaging results are shown (horizontal order) over 10 slices at LV, myocardial signal maximum, and as a temporal intensity profile at a midventricular slice, indicated by blue frame and dashed line. Average heart rate and maximum displacement were 70 bpm and 20 mm, respectively

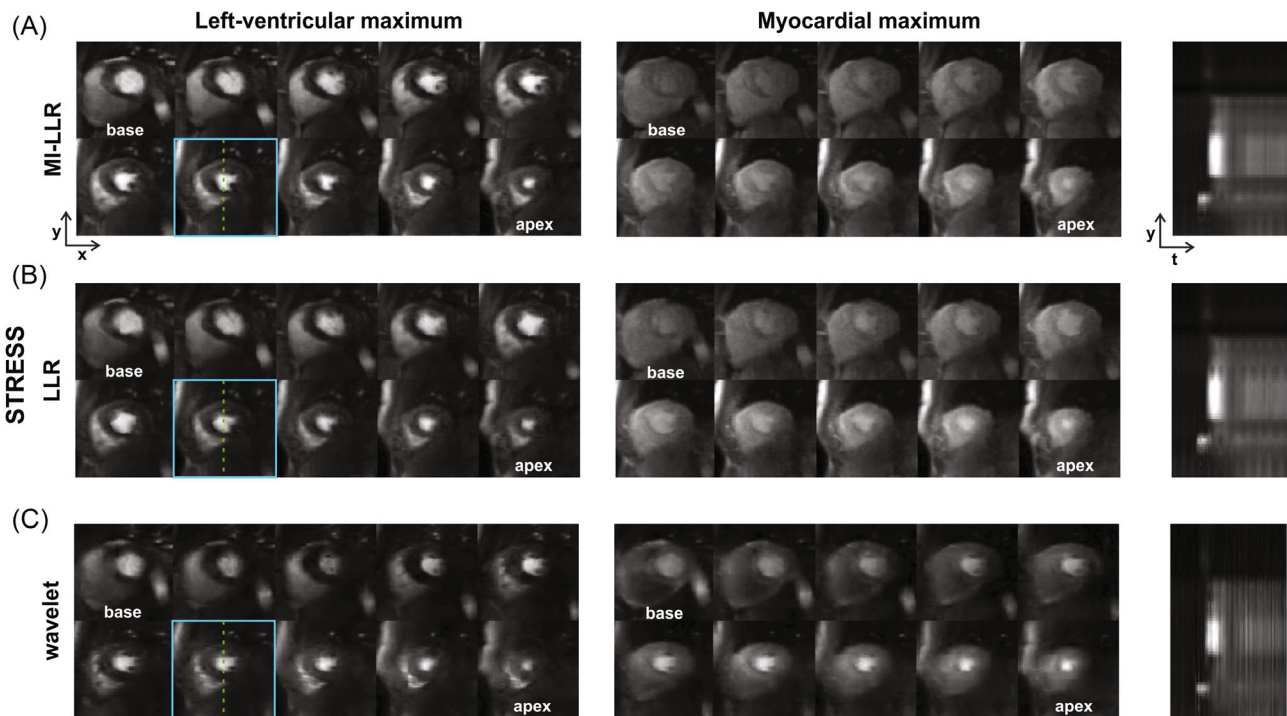


FIGURE 7 In-vivo results for motion-informed locally low-rank (MI-LLR) (A), LLR (B) and ℓ_1 -wavelet (wavelet) (C) during stress condition. Imaging results are shown (horizontal order) over 10 slices at LV, myocardial signal maximum, and as a temporal intensity profile at a midventricular slice, indicated by blue frame and dashed line. Average stress heart rate and maximum displacement were 81 bpm and 24 mm, respectively

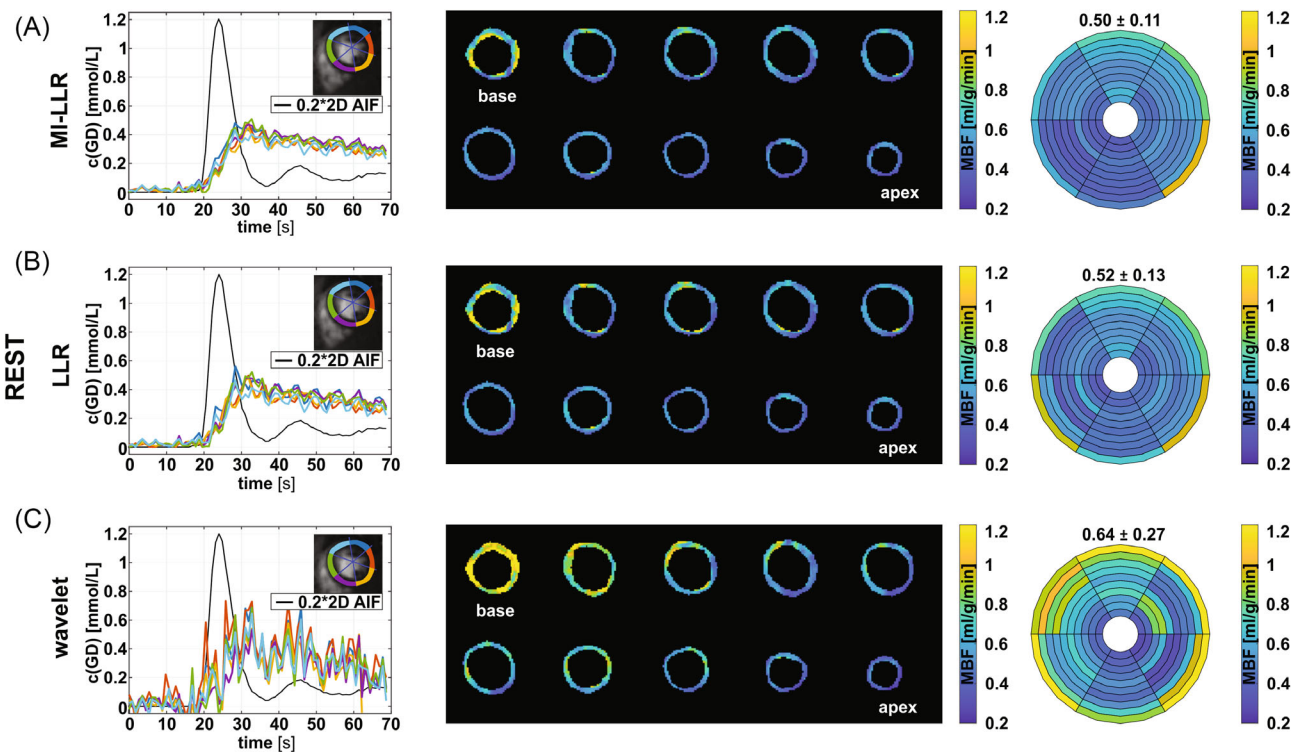


FIGURE 8 Quantification of in-vivo results during rest resulting from motion-informed locally low-rank (MI-LLR) (A), LLR (B) and ℓ_1 -wavelet (wavelet) (C) data of the volunteer presented in Figure 6. The results in panels show (horizontal order) mean concentration time curves over myocardial sectors from midventricular slice (indicated by blue frame in Figure 6) with the 2D arterial input function (AIF), myocardial blood flow (MBF) maps, and regional means with MBF \pm SD. Average resting heart rate and maximum displacements were 70 bpm and 20 mm, respectively

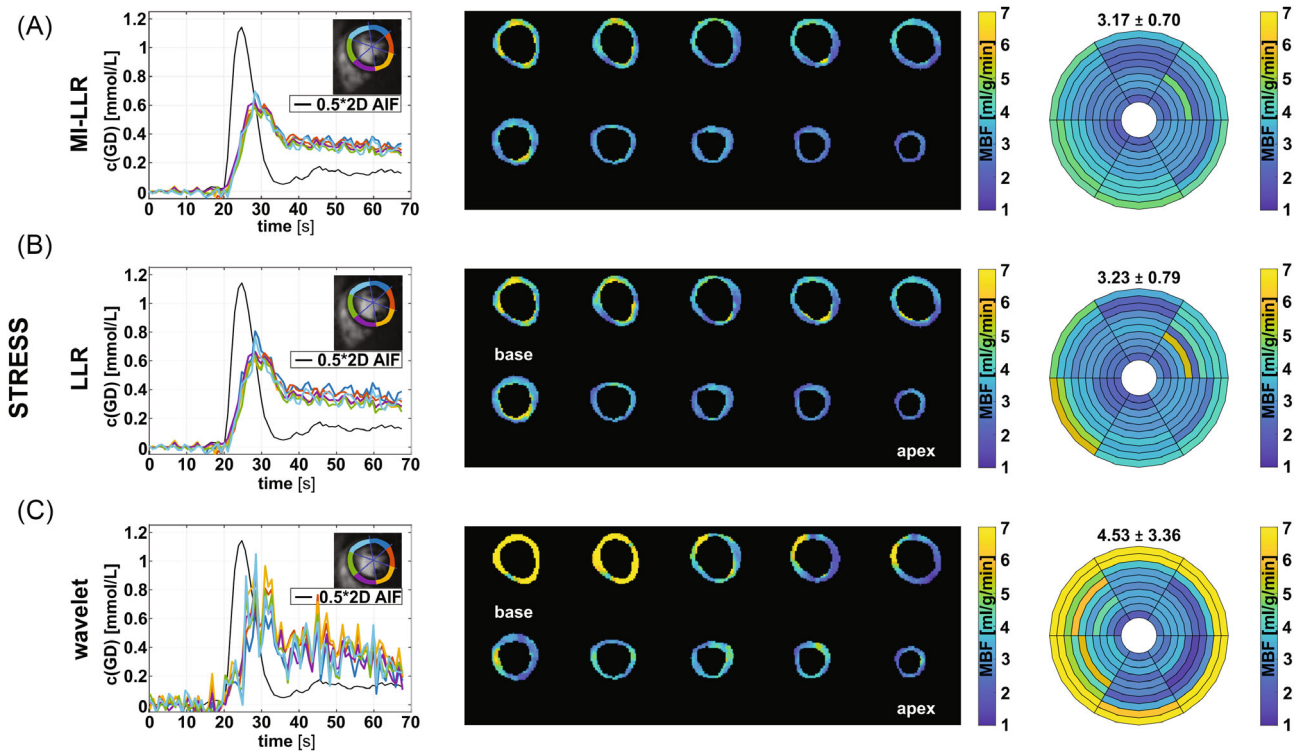


FIGURE 9 Quantification of in-vivo results during stress resulting from motion-informed locally low-rank (MI-LLR) (A), LLR (B), and ℓ_1 -wavelet (wavelet) (C) data of the volunteer presented in Figure 7. The results in panels show (horizontal order) mean concentration time curves over myocardial sectors from midventricular slice (indicated by blue frame in Figure 7) with the 2D arterial input function (AIF), myocardial blood flow (MBF) maps, and regional means with $\text{MBF} \pm \text{SD}$. Average stress heart rate and maximum displacements were 81 bpm at 24 mm, respectively

Especially in simulation, MI-LLR reduces signal elevations in the septal region as caused by high contrast signal from the right-ventricular and LV blood pools. The visually apparent trend for underestimation in the infero-lateral regions is relative to the sites of increased signal which are observed predominantly in basal slices.

In order to relate MI-LLR and LLR to methods commercially available on clinical MR systems, frame-by-frame ℓ_1 compressed sensing with wavelets as sparsifying transform and coil encoding was used, which resulted in significant image distortions and erroneous MBF quantification. The Cartesian pseudo spiral in-out sampling pattern used in the present work ensured that the central k-space was always covered halfway during the acquisition window. This differs from other work that promotes motion robustness by means of radial sampling strategies,^{41,42,77} where the central k-space is traversed by every profile and as such is susceptible to variations in motion state throughout the acquisition, unless this is accounted for by, for example, retrospective binning. Of note, 3D stack-of-stars acquisition schemes inherently demand higher undersampling factors, i.e., $\pi/2$ more data is required in order to fulfil the Nyquist criterion when compared to Cartesian sampling.^{9,41} Possible reduction of the acquisition window by means of

partial echo and partial Fourier sampling as used in other studies^{28,41} was avoided as the approximated Hermitian symmetry is potentially violated by the local modulation of signal phase due to the CA.⁷⁸ However, cardiac motion during the acquisition could have contributed to Gibbs ringing, i.e., dark-rim artefacts,⁷⁹ which were observed in some cases in this study (e.g. Supporting Information Video S2).

Conversion of signal intensities to concentrations requires a signal model. Phantom validation (Figure 5) of MI-LLR signal intensity to concentration conversion showed good agreement within precision of experiment in the range of expected myocardial gadobutrol concentrations from 0.1 to 2.3 mmol/L and motion amplitudes of 30 mm.

Simulation studies using the MRXCAT framework confirmed sufficient robustness of MI-LLR at higher heart rates and breathing amplitudes and was shown to outperform LLR and ℓ_1 -wavelet over a realistic SNR range. MBF quantification from MI-LLR reconstruction showed reduced variability in apical and basal sectors, as well as reduced overestimation of midventricular, infero- and anteroseptal regions. The investigated respiratory amplitudes of 25 and 40 mm in feet-head direction were taken from recorded in-vivo respiratory motion

amplitudes as shown in Supporting Information Figure S2; other work only considered amplitudes of 1.7 and ~ 8 mm.^{30,42} In the simulation studies, sinusoidal breathing patterns of 4.5 s cycle duration were assumed; especially under stress, more irregular and abrupt breathing patterns might occur. In these cases, the exact implications of sudden motion on quantification accuracy remain to be quantified.

It is noted that the perfusion model (Equation 7) fitting problem is reasonably well posed, i.e., three model parameters are fitted considering approximately 40 time points per pixel (the exact value depends on the time span of the first pass and thus the shape of the curve). Therefore, no clear trend in MBF accuracy vs. heart rate or SNR could be detected, contrary to reconstruction nRMSEs (Figure 4A–C). However, systematic bias is intrinsic to each of the considered methods; therefore, a significant improvement of MI-LLR compared to LLR in terms of MBF accuracy was seen in the simulation studies. In the future, a blood tissue exchange model (BTEX) with four free parameters modelled as partial differential equations should be tried as proposed in other work.^{80,81} In that case, superiority of MI-LLR motion compensation is expected to improve quantification robustness more profoundly than shown for the Fermi-based fitting.

In image reconstruction, the patch size as well as the range of regularization parameters λ were determined empirically and found to be generalizable to all datasets. A reference ground truth image could alternatively be used to optimize λ s,⁸² the acquisition of which is, however, hampered by the residual CA in the tissue and the resulting change in contrast. The effects of regularization and image registration used on net spatiotemporal resolution are yet to be determined. Although simulation and in-vivo results show motion robustness of the proposed reconstruction, maximum scan acceleration factors to reduce the influence of intra-shot cardiac motion contributions remain to be investigated. Previous work exploiting motion information for 3D perfusion imaging utilized uniform Cartesian k-t undersampling³⁰ in conjunction with ℓ_2 based regularization, as opposed to non-uniform k-t undersampling and nuclear norm regularization used here. As a result of ℓ_2 -regularization, temporal blurring was observed compromising MBF quantification.³⁰ A comparison of different quantitative free-breathing perfusion approaches (i.e., data acquisition, reconstruction and MBF quantification) for uniform Cartesian, random Cartesian, radial, and spiral undersampling based on synthetic data could be beneficial and will be subject of future work.

Relating to previous work that uses motion correction with LLR, the BLOSM approach is similar to the proposed MI-LLR strategy but was only applied in the context of 2D data⁵³; through-plane motion from true

3D acquisitions was not investigated. Continuous Radial Interleaved simultaneous Multi-slice acquisition at sPoiled steady-state (CRIMP) achieves whole-heart coverage combining self-gating and patch tracking in a continuous multiband acquisition, which uses dual bolus injections for MBF quantification.⁴²

Computation times for the entire reconstruction were on the order of ~ 15 min per scan using a hybrid CPU-GPU implementation. Processing times are mainly determined by the cost of the 3D image registration steps. Furthermore, currently a five-channel coil is used. For larger numbers of receiver channels, the proposed method could be adapted using coil compression methods.⁸³

A limitation of our study is the small number of subjects included. In order to allow for more generalizable statistical results, future studies should enroll larger numbers of subjects without and with suspected coronary artery disease. Diagnostic accuracy should then be addressed in simulation and the in-vivo evaluation. Reader assessment regarding image quality should be investigated. The method was implemented at 1.5T but is applicable to other field strengths.


5 | CONCLUSIONS


The combination of 3D Cartesian pseudo-spiral in-out undersampling in conjunction with motion-informed low-rank reconstruction improves single-bolus free-breathing quantitative 3D myocardial perfusion imaging under rest and stress condition.

ENDNOTE


*Part of the work has been published in the Proceedings of the 30th Annual Meeting of the ISMRM.⁶

ORCID


Tobias Hoh  <https://orcid.org/0000-0002-1391-6347>

Valery Vishnevskiy  <https://orcid.org/0000-0001-5225-5791>

Malgorzata Polacin  <https://orcid.org/0000-0002-0425-5479>

Robert Manka  <https://orcid.org/0000-0002-3383-4998>

Maximilian Fuetterer  <https://orcid.org/0000-0002-7456-1180>

Sebastian Kozerke  <https://orcid.org/0000-0003-3725-8884>

TWITTER

Sebastian Kozerke  @CMR_Zurich

REFERENCES

- Greenwood JP, Maredia N, Younger JF, et al. Cardiovascular magnetic resonance and single-photon emission

- computed tomography for diagnosis of coronary heart disease (CE-MARC): a prospective trial. *Lancet*. 2012;379:453-460.
2. Schwitter J, Wacker CM, Wilke N, et al. MR-IMPACT II: magnetic resonance Imaging for Myocardial Perfusion Assessment in Coronary artery disease Trial: perfusion-cardiac magnetic resonance vs. single-photon emission computed tomography for the detection of coronary artery disease: a comparative multicentre, multivendor trial. *Eur Heart J*. 2013;34:775-781.
 3. Nagel E, Greenwood JP, McCann GP, et al. Magnetic resonance perfusion or fractional flow reserve in coronary disease. *N Engl J Med*. 2019;380:2418-2428.
 4. Jerosch-Herold M, Seethamraju RT, Swingen CM, Wilke NM, Stillman AE. Analysis of myocardial perfusion MRI. *J Magn Reson Imaging*. 2004;19:758-770.
 5. Wilke N, Jerosch-Herold M, Stillman AE, et al. Concepts of myocardial perfusion imaging in magnetic resonance imaging. *Magn Reson Q*. 1994;10:249-286.
 6. Biglands JD, Ibraheem M, Magee DR, Radjenovic A, Plein S, Greenwood JP. Quantitative myocardial perfusion imaging versus visual analysis in diagnosing myocardial ischemia: a CE-MARC substudy. *JACC Cardiovasc Imaging*. 2018;11:711-718.
 7. Hsu LY, Jacobs M, Benovoy M, et al. Diagnostic performance of fully automated pixel-wise quantitative myocardial perfusion imaging by cardiovascular magnetic resonance. *JACC Cardiovasc Imaging*. 2018;11:697-707.
 8. Xue H, Brown LAE, Nilles-Vallespin S, Plein S, Kellman P. Automatic in-line quantitative myocardial perfusion mapping: processing algorithm and implementation. *Magn Reson Med*. 2020;83:712-730.
 9. Fair MJ, Gatehouse PD, DiBella EVR, Firmin DN. A review of 3D first-pass, whole-heart, myocardial perfusion cardiovascular magnetic resonance. *J Cardiovasc Magn Reson*. 2015;17:1-25.
 10. Manka R, Jahnke C, Kozerke S, et al. Dynamic 3-dimensional stress cardiac magnetic resonance perfusion imaging: detection of coronary artery disease and volumetry of myocardial hypoenhancement before and after coronary stenting. *J Am Coll Cardiol*. 2011;57:437-444.
 11. Manka R, Paetsch I, Kozerke S, et al. Whole-heart dynamic three-dimensional magnetic resonance perfusion imaging for the detection of coronary artery disease defined by fractional flow reserve: determination of volumetric myocardial ischaemic burden and coronary lesion location. *Eur Heart J*. 2012;33:2016-2024.
 12. Neumann F-J, Sousa-Uva M, Ahlsson A, et al. 2018 ESC/EACTS Guidelines on myocardial revascularization. *Eur Heart J*. 2019;40:87-165.
 13. Patel AR, Antkowiak PF, Nandalur KR, et al. Assessment of advanced coronary artery disease: advantages of quantitative cardiac magnetic resonance perfusion analysis. *J Am Coll Cardiol*. 2010;56:561-569.
 14. Kotecha T, Chacko L, Chehab O, et al. Assessment of multivessel coronary artery disease using cardiovascular magnetic resonance pixelwise quantitative perfusion mapping. *JACC Cardiovasc Imaging*. 2020;13:2546-2557.
 15. Zorach B, Shaw PW, Bourque J, et al. Quantitative cardiovascular magnetic resonance perfusion imaging identifies reduced flow reserve in microvascular coronary artery disease. *J Cardiovasc Magn Reson*. 2018;20:14.
 16. Kotecha T, Martinez-Naharro A, Boldrini M, et al. Automated pixel-wise quantitative myocardial perfusion mapping by CMR to detect obstructive coronary artery disease and coronary microvascular dysfunction: validation against invasive coronary physiology. *JACC Cardiovasc Imaging*. 2019;12:1958-1969.
 17. Camaioni C, Knott KD, Augusto JB, et al. Inline perfusion mapping provides insights into the disease mechanism in hypertrophic cardiomyopathy. *Heart*. 2020;106:824-829.
 18. Tsao J, Boesiger P, Pruessmann KP. k-t BLAST and k-t SENSE: dynamic MRI with high frame rate exploiting spatiotemporal correlations. *Magn Reson Med*. 2003;50:1031-1042.
 19. Kozerke S, Tsao J, Razavi R, Boesiger P. Accelerating cardiac cine 3D imaging using k-t BLAST. *Magn Reson Med*. 2004;52:19-26.
 20. Tsao J, Kozerke S. MRI temporal acceleration techniques. *J Magn Reson Imaging*. 2012;36:543-560.
 21. Pedersen H, Kozerke S, Ringgaard S, Nehrke K, Won YK. K-t PCA: temporally constrained k-t BLAST reconstruction using principal component analysis. *Magn Reson Med*. 2009;62:706-716.
 22. Vitanis V, Manka R, Giese D, et al. High resolution three-dimensional cardiac perfusion imaging using compartment-based k-t principal component analysis. *Magn Reson Med*. 2011;65:575-587.
 23. Jogiya R, Kozerke S, Morton G, et al. Validation of dynamic 3-dimensional whole heart magnetic resonance myocardial perfusion imaging against fractional flow reserve for the detection of significant coronary artery disease. *J Am Coll Cardiol*. 2012;60:756-765.
 24. Motwani M, Kidambi A, Sourbron S, et al. Quantitative three-dimensional cardiovascular magnetic resonance myocardial perfusion imaging in systole and diastole. *J Cardiovasc Magn Reson*. 2014;16:1-11.
 25. Jogiya R, Morton G, De Silva K, et al. Ischemic burden by 3-dimensional myocardial perfusion cardiovascular magnetic resonance: comparison with myocardial perfusion scintigraphy. *Circ Cardiovasc Imaging*. 2014;7:647-654.
 26. Manka R, Wissmann L, Gebker R, et al. Multicenter evaluation of dynamic three-dimensional magnetic resonance myocardial perfusion imaging for the detection of coronary artery disease defined by fractional flow reserve. *Circ Cardiovasc Imaging*. 2015;8:1-7.
 27. Hamada S, Gotschy A, Wissmann L, et al. Multi-centre study of whole-heart dynamic 3D cardiac magnetic resonance perfusion imaging for the detection of coronary artery disease defined by fractional flow reserve: gender based analysis of diagnostic performance. *Eur Heart J Cardiovasc Imaging*. 2017;18:1099-1106.
 28. Wissmann L, Niemann M, Gotschy A, Manka R, Kozerke S. Quantitative three-dimensional myocardial perfusion cardiovascular magnetic resonance with accurate two-dimensional arterial input function assessment. *J Cardiovasc Magn Reson*. 2015;17:1-11.
 29. Vitanis V, Manka R, Boesiger P, Pedersen H, Kozerke S. High resolution 3D cardiac perfusion imaging using compartment based k-t PCA. *J Cardiovasc Magn Reson*. 2010;12:174-176.
 30. Schmidt JFM, Wissmann L, Manka R, Kozerke S. Iterative k-t principal component analysis with nonrigid motion correction for dynamic three-dimensional cardiac perfusion imaging. *Magn Reson Med*. 2014;72:68-79.

31. Naresh NK, Haji-Valizadeh H, Aouad PJ, et al. Accelerated, first-pass cardiac perfusion pulse sequence with radial k-space sampling, compressed sensing, and k-space weighted image contrast reconstruction tailored for visual analysis and quantification of myocardial blood flow. *Magn Reson Med.* 2019;81:2632-2643.
32. Pflugi S, Roujol S, Akçakaya M, et al. Accelerated cardiac MR stress perfusion with radial sampling after physical exercise with an MR-compatible supine bicycle ergometer. *Magn Reson Med.* 2015;74:384-395.
33. Neimatallah MA, Chenevert TL, Carlos RC, et al. Subclavian MR arteriography: reduction of susceptibility artifact with short echo time and dilute gadopentetate dimeglumine. *Radiology.* 2000;217:581-586.
34. Chen L, Adluru G, Schabel MC, McGann CJ, Dibella EVR. Myocardial perfusion MRI with an undersampled 3D stack-of-stars sequence. *Med Phys.* 2012;39:5204-5211.
35. Fair MJ, Gatehouse PD, Reyes E, et al. Initial investigation of free-breathing 3D whole-heart stress myocardial perfusion MRI. *Glob Cardiol Sci Pract.* 2020;2020:e202038.
36. Kholmovski EG, DiBella EVR. Perfusion MRI with radial acquisition for arterial input function assessment. *Magn Reson Med.* 2007;57:821-827.
37. Salerno M, Sica C, Kramer CM, Meyer CH. Improved first-pass spiral myocardial perfusion imaging with variable density trajectories. *Magn Reson Med.* 2013;70:1369-1379.
38. Shin T, Nayak KS, Santos JM, Nishimura DG, Hu BS, McConnell MV. Three-dimensional first-pass myocardial perfusion MRI using a stack-of-spirals acquisition. *Magn Reson Med.* 2013;69:839-844.
39. Salerno M, Sica CT, Kramer CM, Meyer CH. Optimization of spiral-based pulse sequences for first-pass myocardial perfusion imaging. *Magn Reson Med.* 2011;65:1602-1610.
40. Wang H, Bangerter NK, Park DJ, et al. Comparison of centric and reverse-centric trajectories for highly accelerated three-dimensional saturation recovery cardiac perfusion imaging. *Magn Reson Med.* 2015;74:1070-1076.
41. Mendes JK, Adluru G, Likhite D, et al. Quantitative 3D myocardial perfusion with an efficient arterial input function. *Magn Reson Med.* 2020;83:1949-1963.
42. Tian Y, Mendes J, Wilson B, et al. Whole-heart, ungated, free-breathing, cardiac-phase-resolved myocardial perfusion MRI by using Continuous Radial Interleaved simultaneous Multi-slice acquisitions at sPoiled steady-state (CRIMP). *Magn Reson Med.* 2020;84:3071-3087.
43. Pan JA, Robinson AA, Yang Y, et al. Diagnostic accuracy of spiral whole-heart quantitative adenosine stress cardiovascular magnetic resonance with motion compensated L1-SPIRIT. *J Magn Reson Imaging.* 2021;54:1268-1279.
44. Wissmann L, Gotschy A, Santelli C, et al. Analysis of spatiotemporal fidelity in quantitative 3D first-pass perfusion cardiovascular magnetic resonance. *J Cardiovasc Magn Reson.* 2017;19:1-15.
45. Scannell CM, Villa ADM, Lee J, Breeuwer M, Chiribiri A. Robust non-rigid motion compensation of free-breathing myocardial perfusion MRI data. *IEEE Trans Med Imaging.* 2019;38:1812-1820.
46. Likhite D, Adluru G, Hu N, McGann C, Dibella E. Quantification of myocardial perfusion with self-gated cardiovascular magnetic resonance. *J Cardiovasc Magn Reson.* 2015;17:1-15.
47. Adluru G, McGann C, Speier P, Kholmovski EG, Shaaban A, Dibella EVR. Acquisition and reconstruction of undersampled radial data for myocardial perfusion magnetic resonance imaging. *J Magn Reson Imaging.* 2009;29:466-473.
48. Feng L, Axel L, Chandarana H, Block KT, Sodickson DK, Otazo R. XD-GRASP: golden-angle radial MRI with reconstruction of extra motion-state dimensions using compressed sensing. *Magn Reson Med.* 2016;75:775-788.
49. Haji-Valizadeh H, Guo R, Kucukseymen S, et al. Artifact reduction in free-breathing, free-running myocardial perfusion imaging with interleaved non-selective RF excitations. *Magn Reson Med.* 2021;86:954-963.
50. Batchelor PG, Atkinson D, Irarrazaval P, Hill DLG, Hajnal J, Larkman D. Matrix description of general motion correction applied to multishot images. *Magn Reson Med.* 2005;54:1273-1280.
51. Zhou R, Huang W, Yang Y, et al. Simple motion correction strategy reduces respiratory-induced motion artifacts for k-t accelerated and compressed-sensing cardiovascular magnetic resonance perfusion imaging. *J Cardiovasc Magn Reson.* 2018;20:1-13.
52. Akçakaya M, Basha TA, Pflugi S, et al. Localized spatio-temporal constraints for accelerated CMR perfusion. *Magn Reson Med.* 2014;72:629-639.
53. Chen X, Salerno M, Yang Y, Epstein FH. Motion-compensated compressed sensing for dynamic contrast-enhanced MRI using regional spatiotemporal sparsity and region tracking: block low-rank sparsity with motion-guidance (BLOSM). *Magn Reson Med.* 2014;72:1028-1038.
54. Liu J, Jin S, Li Q, et al. Motion compensation combining with local low rank regularization for low dose dynamic CT myocardial perfusion reconstruction. *Phys Med Biol.* 2021;66:145007.
55. Zhang T, Pauly JM, Levesque IR. Accelerating parameter mapping with a locally low rank constraint. *Magn Reson Med.* 2015;73:655-661.
56. Cruz G, Qi H, Jaubert O, et al. Generalized low-rank nonrigid motion-corrected reconstruction for MR fingerprinting. *Magn Reson Med.* 2022;87:746-763.
57. Gatehouse PD, Elkington AG, Ablitt NA, Yang G-Z, Pennell DJ, Firmin DN. Accurate assessment of the arterial input function during high-dose myocardial perfusion cardiovascular magnetic resonance. *J Magn Reson Imaging.* 2004;20:39-45.
58. Milidonis X, Franks R, Schneider T, et al. Influence of the arterial input sampling location on the diagnostic accuracy of cardiovascular magnetic resonance stress myocardial perfusion quantification. *J Cardiovasc Magn Reson.* 2021;23:35.
59. Liu B, Zou YM, Ying L. Sparsesense: Application of compressed sensing in parallel MRI. In: 2008 International Conference on Information Technology and Applications in Biomedicine. 2008. p. 127-130.
60. Liang D, Liu B, Wang J, Ying L. Accelerating SENSE using compressed sensing. *Magn Reson Med.* 2009;62:1574-1584.
61. Hoh T, Vishnevskiy V, Fuetterer M & Kozerke S. Free-breathing motion-informed quantitative 3D myocardial perfusion imaging. In: Proceedings of the 30th annual meeting of the ISMRM. 2021;0049.
62. Ogg RJ, Kingsley PB, Taylor JS. WET, a T1- and B1-insensitive water-suppression method for in vivo localized 1H NMR spectroscopy. *J Magn Reson Ser B.* 1994;104:1-10.

63. Lustig M, Donoho D, Pauly JM. Sparse MRI: the application of compressed sensing for rapid MR imaging. *Magn Reson Med.* 2007;58:1182-1195.
64. Ravishankar S, Ye JC, Fessler JA. Image reconstruction: from sparsity to data-adaptive methods and machine learning. *Proc IEEE.* 2020;108:86-109.
65. Nesterov YE. A method for solving the convex programming problem with convergence rate $O(1/k^2)$. *Dokl Akad Nauk SSSR.* 1983;269:543-547.
66. Vishnevskiy V, Gass T, Szekely G, Tanner C, Goksel O. Isotropic total variation regularization of displacements in parametric image registration. *IEEE Trans Med Imaging.* 2017;36:385-395.
67. Huizinga W, Poot DHJ, Guyader J-M, et al. PCA-based group-wise image registration for quantitative MRI. *Med Image Anal.* 2016;29:65-78.
68. Blomgren P, Chan TF. Color TV: total variation methods for restoration of vector-valued images. *IEEE Trans Image Process.* 1998;7:304-309.
69. Uecker M, Lai P, Murphy MJ, et al. ESPIRiT—an eigenvalue approach to autocalibrating parallel MRI: where SENSE meets GRAPPA. *Magn Reson Med.* 2014;71:990-1001.
70. Otazo R, Kim D, Axel L, Sodickson DK. Combination of compressed sensing and parallel imaging for highly accelerated first-pass cardiac perfusion MRI. *Magn Reson Med.* 2010;64:767-776.
71. Hollingsworth KG. Reducing acquisition time in clinical MRI by data undersampling and compressed sensing reconstruction. *Phys Med Biol.* 2015;60:R297-R322.
72. Tamir JI, Ong F, Cheng JY, Uecker M, Lustig M. Generalized magnetic resonance image reconstruction using the Berkeley advanced reconstruction toolbox. In: Proceedings of the ISMRM 2016 data sampling and image reconstruction workshop. 2016. p. 9660006.
73. Brix G, Schad LR, Deimling M, Lorenz WJ. Fast and precise T1 imaging using a TOMROP sequence. *Magn Reson Imaging.* 1990;8:351-356.
74. Jerosch-herold M, Wilke N, Stillman AE, et al. Magnetic resonance quantification of the myocardial perfusion reserve with a Fermi function model for constrained deconvolution. *Med Physiol.* 1998;25:73-84.
75. Messroghli DR, Radjenovic A, Kozerke S, Higgins DM, Sivananthan MU, Ridgway JP. Modified look-locker inversion recovery (MOLLI) for high-resolution T1 mapping of the heart. *Magn Reson Med.* 2004;52:141-146.
76. Wissmann L, Santelli C, Segars WP, Kozerke S. MRXCAT: realistic numerical phantoms for cardiovascular magnetic resonance. *J Cardiovasc Magn Reson.* 2014;16:63.
77. Ferrazzi G, McElroy S, Neji R, et al. All-systolic first-pass myocardial rest perfusion at a long saturation time using simultaneous multi-slice imaging and compressed sensing acceleration. *Magn Reson Med.* 2021;86:663-676.
78. Akbudak E, Norberg RE, Conturo TE. Contrast-agent phase effects: an experimental system for analysis of susceptibility, concentration, and bolus input function kinetics. *Magn Reson Med.* 1997;38:990-1002.
79. Di Bella EVR, Parker DL, Sinusas AJ. On the dark rim artifact in dynamic contrast-enhanced MRI myocardial perfusion studies. *Magn Reson Med.* 2005;54:1295-1299.
80. Bassingthwaite JB, Wang CY, Chan IS. Blood-tissue exchange via transport and transformation by capillary endothelial cells. *Circ Res.* 1989;65:997-1020.
81. Kellman P, Hansen MS, Nielles-Vallespin S, et al. Myocardial perfusion cardiovascular magnetic resonance: optimized dual sequence and reconstruction for quantification. *J Cardiovasc Magn Reson.* 2017;19:43.
82. Walheim J, Dillinger H, Kozerke S. Multipoint 5D flow cardiovascular magnetic resonance—accelerated cardiac- and respiratory-motion resolved mapping of mean and turbulent velocities. *J Cardiovasc Magn Reson.* 2019;21:1-13.
83. Buehrer M, Pruessmann KP, Boesiger P, Kozerke S. Array compression for MRI with large coil arrays. *Magn Reson Med.* 2007;57:1131-1139.

SUPPORTING INFORMATION

Additional supporting information may be found in the online version of the article at the publisher's website.

Table S1 Mean \pm SD of contrast agent concentration at peak myocardial enhancement.

FIGURE S1 Motion-informed locally low-rank (MI-LLR) image reconstruction using in-vivo data obtained during stress condition (c.f. Figure 7). Patch-based initial LLR reconstruction followed by full FOV registration to obtain deformation fields, which are subsequently inverted to allow for regularization over motion states. The resulting full FOV 3D image series still contains motion as indicated by the intensity-time profiles and hence require registration in the reduced FOV for myocardial blood flow (MBF) quantification. For every step, corresponding intensity-time profiles are depicted. Average heart rate and maximum displacement were 81 bpm and 24 mm, respectively

FIGURE S2 In-vivo breathing motion for all volunteers. Maximum amplitude of displacement per imaging series at respective mean heart rate is shown in (A). The respiratory period at respective heart rate is shown in (B). Dashed line serves as guide to the eye and separates data points from measurements obtained at rest and stress

FIGURE S3 Myocardial blood flow (MBF) means with MBF \pm SD from 60 circumferential regions during rest and stress condition reconstructed with the proposed motion-informed locally low rank reconstruction (MI-LLR) for all subjects. All volunteers on the right side of the dashed line received a rest and stress protocol

FIGURE S4 In-vivo results for example case with unusually high heart rate and respiratory amplitude for motion-informed locally low-rank reconstruction (MI-LLR) (A), LLR (B) and ℓ_1 -wavelet (wavelet) (C) during rest condition. The panel shows (horizontal order) reconstruction magnitude image at a midventricular slice at left-ventricular signal maximum, corresponding intensity-time profiles, mean concentration time curves

over myocardial sectors with the 2D arterial input function (AIF), resulting myocardial blood flow (MBF) maps (D) and regional means with $MBF \pm SD$, respectively. Average heart rate and maximum displacement were 80 bpm and 26 mm, respectively

FIGURE S5 In-vivo results for example case with comparatively low respiratory amplitude for motion-informed locally low-rank (MI-LLR) (A), LLR (B) and ℓ_1 -wavelet (wavelet) (C) during rest condition. Imaging results are shown (horizontal order) as magnitude image time series over ten slices at left-ventricular, myocardial signal maximum and as a temporal intensity profile at a midventricular slice, indicated by blue frame and dashed line. Average heart rate and maximum displacements were, 61 bpm at 12 mm, respectively

FIGURE S6 In-vivo results for example case with comparatively low respiratory amplitude for motion-informed locally low-rank (MI-LLR) (A), LLR (B) and ℓ_1 -wavelet (wavelet) (C) during stress condition. Imaging results are shown (horizontal order) as magnitude image time series over ten slices at left-ventricular, myocardial signal maximum and as a temporal intensity profile at a midventricular slice, indicated by blue frame and dashed line. Average stress heart rate and maximum displacements were, 78 bpm at 17 mm, respectively

FIGURE S7 Quantification of in-vivo results for example case with comparatively low respiratory amplitude during rest resulting from motion-informed locally low-rank (MI-LLR) (A), LLR (B) and ℓ_1 -wavelet (wavelet) (C) data. The results in panels show (horizontal order), mean concentration time curves over myocardial sectors from midventricular slice (indicated by blue frame in Figure S4) with the 2D arterial input function (AIF), myocardial blood flow (MBF) maps and regional means, with $MBF \pm SD$, respectively. Average resting heart rate and maximum displacements were, 61 bpm at 12 mm, respectively

FIGURE S8 Quantification of in-vivo results for example case with comparatively low respiratory amplitude during stress resulting from motion-informed locally low-rank (MI-LLR) (A), LLR (B) and ℓ_1 -wavelet (wavelet) (C) data. The results in panels show (horizontal order), mean concentration time curves over myocardial sectors from midventricular slice (indicated by blue frame in Figure S6) with the 2D arterial input function (AIF),

myocardial blood flow (MBF) maps and regional means, with $MBF \pm SD$, respectively. Average stress heart rate and maximum displacements were, 78 bpm at 17 mm, respectively

VIDEO S1 In-vivo motion-informed locally low-rank reconstruction (MI-LLR), LLR and ℓ_1 -wavelet (wavelet) data during rest condition shown as animated magnitude image time series over all slices (MI-LLR, LLR and wavelet from top to bottom rows; horizontal order is base to apex). Corresponding results are shown in Figures 6 and 8. Average resting heart rate and maximum displacements were 70 bpm and 20 mm, respectively

VIDEO S2 In-vivo motion-informed locally low-rank reconstruction (MI-LLR), LLR and ℓ_1 -wavelet (wavelet) data during stress condition shown as animated magnitude image time series over all slices (MI-LLR, LLR and wavelet from top to bottom rows; horizontal order is base to apex). Corresponding results are shown in Figures 7 and 9. Average stress heart rate and maximum displacements were 81 bpm and 24 mm, respectively

VIDEO S3 In-vivo motion-informed locally low-rank reconstruction (MI-LLR), LLR and ℓ_1 -wavelet (wavelet) data during rest condition shown as animated magnitude image time series over all slices (MI-LLR, LLR and wavelet from top to bottom rows; horizontal order is base to apex). Corresponding results are shown in Figures S4 and S6. Average resting heart rate and maximum displacements were 61 bpm and 12 mm, respectively

VIDEO S4 In-vivo motion-informed locally low-rank reconstruction (MI-LLR), LLR and ℓ_1 -wavelet (wavelet) data during stress condition shown as animated magnitude image time series over all slices (MI-LLR, LLR and wavelet from top to bottom rows; horizontal order is base to apex). Corresponding results are shown in S5 and S7. Average resting heart rate and maximum displacements were 78 bpm and 17 mm, respectively

How to cite this article: Hoh T, Vishnevskiy V, Polacin M, Manka R, Fuetterer M, Kozerke S. Free-breathing motion-informed locally low-rank quantitative 3D myocardial perfusion imaging. *Magn Reson Med.* 2022;88:1575-1591. doi: 10.1002/mrm.29295